nature water

Article

https://doi.org/10.1038/s44221-023-00131-3

# Spatially separated crystallization for selective lithium extraction from saline water

Received: 5 December 2022

Accepted: 10 August 2023

Published online: 7 September 2023

Check for updates

Xi Chen[1,2,3,7], Meiqi Yang[1,2,7], Sunxiang Zheng[1,2], Fernando Temprano-Coleto[2,4], Qi Dong[5], Guangming Cheng[6], Nan Yao[6], Howard A. Stone[4], Liangbing Hu[5] & Zhiyong Jason Ren[1,2]

Limited lithium supply is hindering the global transformation towards electrification and decarbonization. Current lithium mining can be energy, chemical and land intensive. Here we present an efficient and self-concentrating crystallization method for the selective extraction of lithium from both brine and seawater. The sequential and separable crystallization of cation species with different concentrations and solubilities was enabled by a twisted and slender 3D porous natural cellulose fibre structure via capillary and evaporative flows. The process exhibited an evaporation rate as high as 9.8 kg $m^{-2}$ $h^{-1}$, and it selectively concentrated lithium by orders of magnitude. The composition and spatial distribution of crystals were characterized, and a transport model deciphered the ion re-distribution process in situ. We also demonstrated system scalability via a 100-crystallizer array.

Critical minerals, such as lithium, have become a global development priority due to the exponential demand for such materials for batteries used in electric vehicles, consumer electronics and energy storage systems[1–3]. However, the sustainable supply of lithium can be a major barrier to support this energy transformation[4,5]. Indeed, the price of lithium has skyrocketed by tenfold in the past decade, from US$6,000 per ton in 2016 to nearly US$60,000 per ton in 2022, and the trend and fluctuation are expected to continue[6]. With the fast expansion of this market, the gap between demand and supply will keep increasing, as the demand for lithium is expected to rise from approximately 0.5 million metric tons of lithium carbonate equivalent (LCE) in 2021 to more than 3 million metric tons in 2030 (refs. 7–9). It is therefore imperative to discover new approaches to boost new lithium production rate and capacity, not only from traditional salt lakes and continental brines, which are accessible in very few countries, but also from new sources such as low-concentration oilfield brines and seawater[10]. These new sources contain lower concentrations of lithium but can greatly expand lithium availability and ease geographical constraints[11,12]. For example, oceans contain ~5,000 times more Li than what is found on land, with ~230 billion tons of Li available[13], but the low concentration (~0.2 ppm) makes most extraction technologies unpractical[14].

Currently, almost all lithium mining and production occurs in Latin America, Australia and China, and more than 50% of global lithium is currently produced from continental brines using large multi-stage evaporation ponds[15]. The world's largest pond in Chile produced 20% of the global Li supply in 2019, but this evaporative process takes a long time (15–18 months) and requires a large land area (~32.3 $km^2$) (ref. 16). Additionally, the operation is known to negatively impact local groundwater and ecosystems and has limited capability of processing brine sources with low lithium concentration (for example, <100 ppm) (refs. 17–20). Recently, new processes that perform direct lithium extraction have been developed by flowing brines through Li-selective materials using processes based on adsorption, ion exchange, electrodialysis and solvent extraction[21–25]. These methods show potential for increasing Li recovery and tapping into lower-concentration sources, but they are facing some major barriers in terms of selectivity, energy and chemical uses, and high cost. For example, the emerging electrodialysis with lithium-selective membranes relies on a selective

[1]Department of Civil and Environmental Engineering, Princeton University, Princeton, NJ, USA. [2]Andlinger Center for Energy and the Environment, Princeton University, Princeton, NJ, USA. [3]Now at School of Environment, Tsinghua University, Beijing, China. [4]Department of Mechanical and Aerospace Engineering, Princeton University, Princeton, NJ, USA. [5]Department of Materials Science and Engineering, University of Maryland, College Park, MD, USA. [6]Princeton Materials Institute, Princeton University, Princeton, NJ, USA. [7]These authors contributed equally: Xi Chen, Meiqi Yang.
e-mail: zjren@princeton.edu

https://doi.org/10.1038/s44221-023-00131-3

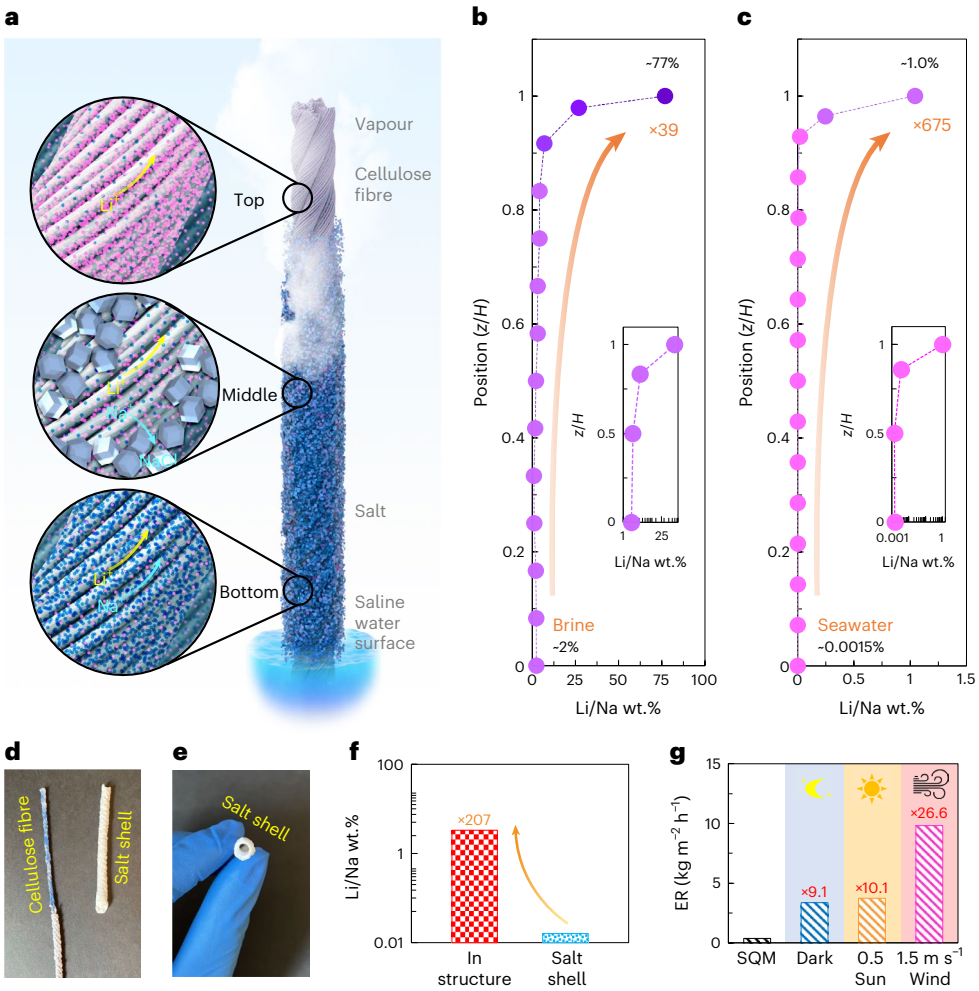


**Fig. 1 | Interfacial crystallization and spatial distribution of ion products on the twisted 3D fibre structure. a**, Schematic of the 3D spatial crystallization process. At the bottom position (Bottom), mixed Li and Na ions are carried upward via capillary flow. At the middle position (Middle), NaCl saturates and crystallizes, while Li species continue to move upward with the water flow. At the top position (Top), Li ions precipitate when the saline water completely evaporates. **b**,**c**, The Li/Na ratio increased along the 3D fibre crystallizer, with Li concentrated by >39 times at the top when using brine (**b**) and >675 times at the top when using seawater (**c**). Note that all Li/Na ratios along the height of the crystallizer were measured after removing the salt shell (details in the following section), exhibiting the Li separation performance within the crystallizer's porous structure. **d**,**e**, A Na-rich salt shell forms on the outside of the crystallizer, which is easy to separate and harvest physically. **d**, Easy separation between cellulose fiber and the formed salt shell. **e**, Top-view of the separated salt shell. **f**, The Li/Na ratio is >200 times higher than that in the Na-rich salt shell, indicating the spatial separation of Li and Na in the radial direction. **g**, Comparison of the average water ER at the SQM Li production site in Salar de Atacama, Chile (22 °C, RH 22%), and the average ERs of a 100-fibre-crystallizers array in the dark, under 0.5 sun irradiation, or under 1.5 m $s^{-1}$ wind.

ion exchange mechanism, which can result in incomplete extraction of lithium. A study reported a recovery rate of ~20% after 3 h, and the Li/Na selectivity was only 1.3 (refs. 26,27). In addition, electrodialysis employs an electrical field to drive ion exchange, which can be energy intensive. Solvent extraction is another method gaining attraction, as studies reported crown ethers have stronger complexes with $Li^+$ over other cations with a moderate Li/Na selectivity ranging from 2 to 5 (ref. 28). However, current development is hindered by high material costs and the need for large amounts of energy and organic solvents[29–31]. Moreover, after magnesium has been removed using chemical precipitation or electrocoagulation, Li separation from monovalent ions (such as Na) becomes a major barrier[17–20].

In this Article, we report a passive method for fast and selective extraction of lithium from saline water based on twisted cellulose fibre crystallizers. By taking advantage of the high solubility and mobility of lithium salts in water[32], we fabricated the crystallizers with unique porosity, tortuosity and hydrophilicity, which enabled selective extraction and spatial separation of lithium from other ions for simple harvesting (Fig. 1a). We show this crystallizer can accelerate the evaporation speed by more than 20 times compared with evaporation ponds, potentially reducing the operation time from >15 months to <20 days if properly scaled up. Moreover, compared with traditional evaporation, the process can selectively concentrate lithium by over 39- and 675-fold from continental brine and seawater, respectively.

## Results

The sequential and separable precipitation of lithium from sodium of different initial concentrations and solubilities is made possible by capillary and evaporative flows within the fibre crystallizer. The porous structure can raise water by ~0.6 m via the capillary force and allows for fast water evaporation on the side surfaces. As water evaporates, salts with higher concentrations and lower solubilities, like NaCl, crystallize at lower heights of the fibre crystallizer, while salts with lower concentrations and higher solubilities, like LiCl, move further upward and precipitate near the top (Fig. 1a). Therefore, with sufficient height of the twisted fibre structure, different salts reach their saturation points

at different locations and precipitate sequentially along the crystallizer, providing enough spatial separation for recovery. Figure 1b shows that, during evaporation operation, Li/Na wt. gradually increases along with the crystallizer height ($H$), and after 60 h, the Li/Na wt. (that is, 77%) at the top of the crystallizer is 39 times higher than the typical continental Li-containing brine (that is, 2%). The average selectivity of Li versus Na on the top 10% length of the crystallizer was 34.5 ± 5.1, while the average selectivity over the whole length was 7.1 ± 1.2. In total, the lithium recovery by the whole length of the crystallizer was 87.2 ± 1.9%, in which 9.2 ± 4.1% was accumulated on the top 10% length (Supplementary Fig. 1). A best recovery strategy that balances purity and quantity would consider the final product need, and multi-stage evaporation could be implemented to increase both. When using seawater, the crystallizer could raise Li/Na wt. by >675 times (that is, from 0.0015% to 1.02%), indicating that such spatial crystallization process can fit a variety of target ion concentration conditions (Fig. 1c). With a two-stage system, the final Li/Na wt. could reach a level comparable with brine-based lithium extraction (Supplementary Fig. 2). We provided more discussions in Supplementary Information regarding the theoretical and practical considerations (Supplementary Note 1).

The spatial separation was also observed along the radial direction ($R$), with a Na-rich salt shell formed outside the crystallizer (Fig. 1d,e). Compared with a very high Na content in the salt shell, the Li/Na wt. was >200 times higher inside the crystallizer structure (Fig. 1f). This enables easy physical separation of Na salts from the crystallizer and further facilitates the recovery of concentrated Li in the porous structure (Supplementary Movie 1). This spatial separation is a result of ion re-distribution within the porous material, which is influenced by the competition between advection and diffusion. With a high evaporation rate (ER) at the surfaces of the crystallizer, advection is dominant, and salts with higher concentration (NaCl) reach saturation first and crystallize at the air–solid interface where drying occurs. When the drying of the water expands from outside to the centre, amorphous Li salts start to precipitate in the centre. This spatial distribution of different salts allows the selective accumulation and separation of lithium from other cations.

In the current design, the crystallizer features a very high height/radius ($H/R$) ratio of ~600, which enables a large surface area and fast ER. A single device (projected area of 0.031 $cm^2$) under an ambient laboratory condition showed an ER of 382 kg $m^{-2}$ $h^{-1}$. An array of 100 crystallizers (projected area 225 $cm^2$) obtained an area normalized ER of 3.4 kg $m^{-2}$ $h^{-1}$ (Supplementary Fig. 3). With 500 W $m^{-2}$ solar radiation, the ER improved to 3.7 kg $m^{-2}$ $h^{-1}$. When tested under the environmental condition simulating the actual weather in the Sociedad Química y Minera de Chile S.A. (SQM) LCE production site at Salar de Atacama, Chile (22 °C, relative humidity (RH) 22%, 1.5 m $s^{-1}$ wind, dark), the 100 crystallizers array showed an ER of 9.8 kg $m^{-2}$ $h^{-1}$, which is ~27 times faster than the values reported by the largest evaporation ponds for lithium extraction (3,200 mm per year, SQM, Salar de Atacama, Chile)[33] (Fig. 1g). This suggests that the system can greatly shorten the operation time of the evaporation ponds, potentially from >15 months to <20 days if properly scaled up. The increased ER may further improve ion selectivity per our mechanistic model, and details can be found in later sections.

The demonstrated crystallizer is made from natural cellulose fibres fabricated with four twisted strings (Fig. 2a). A 3D X-ray scanning image shows the cross-section of the 3D structure, where four strings are twisted tightly with an angle of ~23–24° to the vertical (Fig. 2b, Supplementary Fig. 4 and Supplementary Movie 2). When a 70-cm-long crystallizer was partially dipped in saline water, evaporation occurs continuously along the water lifting height ($H$) (Fig. 2c). Figure 2d shows the crystallization from brine after 60 h in ambient conditions. It was observed that most of the NaCl crystals formed surrounding the surface of the structure at around 1/3 height, while salt layers became gradually thinner upward (Fig. 2d). A time lapse video records that different original salt concentrations may result in different crystallization heights (Supplementary Movie 3).

To decipher the composition and the mechanisms of sequential crystallization of different salt species, we characterized the salt density distribution on two representative sections, one is at the very top (location 1) and another is at the top of the thickest salt accumulation (location 2) (Fig. 2d). The 3D X-ray images reveal the very different salt densities and distributions between the two locations (Fig. 2e). The most observable difference is in the longitudinal direction, the salt density was much higher at the location 2 than location 1, as evidenced by the colour change from red to blue. In addition, there is a density gradient in the radial direction, with lower densities inside the structure, while higher densities outside the structure. This supports the hypothesis that Li salt is enriched inside the structure, while Na salt is enriched outside the surface. This distribution was further confirmed by other advanced elemental scanning methods. Overall, along the H direction, much higher Li/Na (>77%) was identified on the very top location, while lower Li/Na (~1.0–4.3%) was found in the lower 0.85 H section, with large NaCl cubic crystals dominating the formation of a thick salt shell.

We developed a mechanistic model to describe the ion transport inside the slender porous structure, which continuously draws liquid from the reservoir and evaporates along its length (Fig. 2g). The model predicts the concentration of Na ($c_{Na}$) or Li ($c_{Li}$) as a function of time $t$ and the position $z$ along the water lifting height, $H$ (Fig. 2h). The detailed model construction can be found in Methods. The predicted concentrations critically depend on the effective Péclet number $\mathrm{Pe} = jH^2/(\rho \mathrm{DR})$, a dimensionless parameter quantifying the ratio between advection and diffusion. Given the very high $H/R$, advection is dominant, causing an exponential increase in the concentration of both ions at the top of the crystallizer, $c(z = H) = c^0 e^{2tj/(\rho R)}$. Such a sharp buildup of concentration, combined with the fact that Na is much closer to saturation in the bulk solution ($c^0_{Na}/c^{sat}_{Na} \gg c^0_{Li}/c^{sat}_{Li}$), leads to rapid precipitation of sodium. Consequently, after a characteristic time $(\rho R/2j)\ln\left(c^{sat}_{Na}/c^0_{Na}\right)$, the $c_{Na}$ remains constant at the top of the crystallizer, in equilibrium with the NaCl salt. This allows Li, which is comparatively further from saturation, to increase its relative concentration (Fig. 2i) as evaporation keeps driving the solution through the porous NaCl salt shell. Model results are consistent with our experimental observations (Fig. 1b,c and Supplementary Figs. 5 and 6), showing also a pronounced buildup of Li mostly at the top 10% of the wet crystallizer. Note that, when the ER increases, the maximum Li selectivity can greatly increase on the basis of the model prediction (Supplementary Fig. 7). This indicates that solar incidence and wind gust conditions in the field environment will accelerate evaporation and enhance efficacy compared with the lab condition (Supplementary Note 3).

The experimental results support the hypothesis that in the radial direction ($R$), NaCl crystallizes outside the structure while LiCl concentrates in the centre section (Fig. 3a). This is further supported by the cross-section scanning electron microscopy (SEM) with energy-dispersive X-ray analysis (EDX) scanning, where the Na elemental map shows a circular shape surrounding the crystallizer structure, and the Li map shows a dispersed distribution across the crystallizer's cross-section (Fig. 3b–d). When focusing on the area between the fibres and salt crystals (Fig. 3e, pink box in Fig. 3b), only salt crystals exhibit clear Na spectra, while the fibres showed no Na signal (Fig. 3f). In contrast, Li spectra were detected across the fibre areas, with the weakest signal at the bottom-right corner, where NaCl crystals are located (Fig. 3g). More images and discussion can be found in Supplementary Information, further confirming that NaCl crystals formed outside on the fibre, while LiCl formed amorphous salts across the fibre (Supplementary Figs. 8–10). Such a spatial distribution allows extraction and separation of Li and Na individually in practice, which is demonstrated in crystallizer array testing (Fig. 5).

https://doi.org/10.1038/s44221-023-00131-3

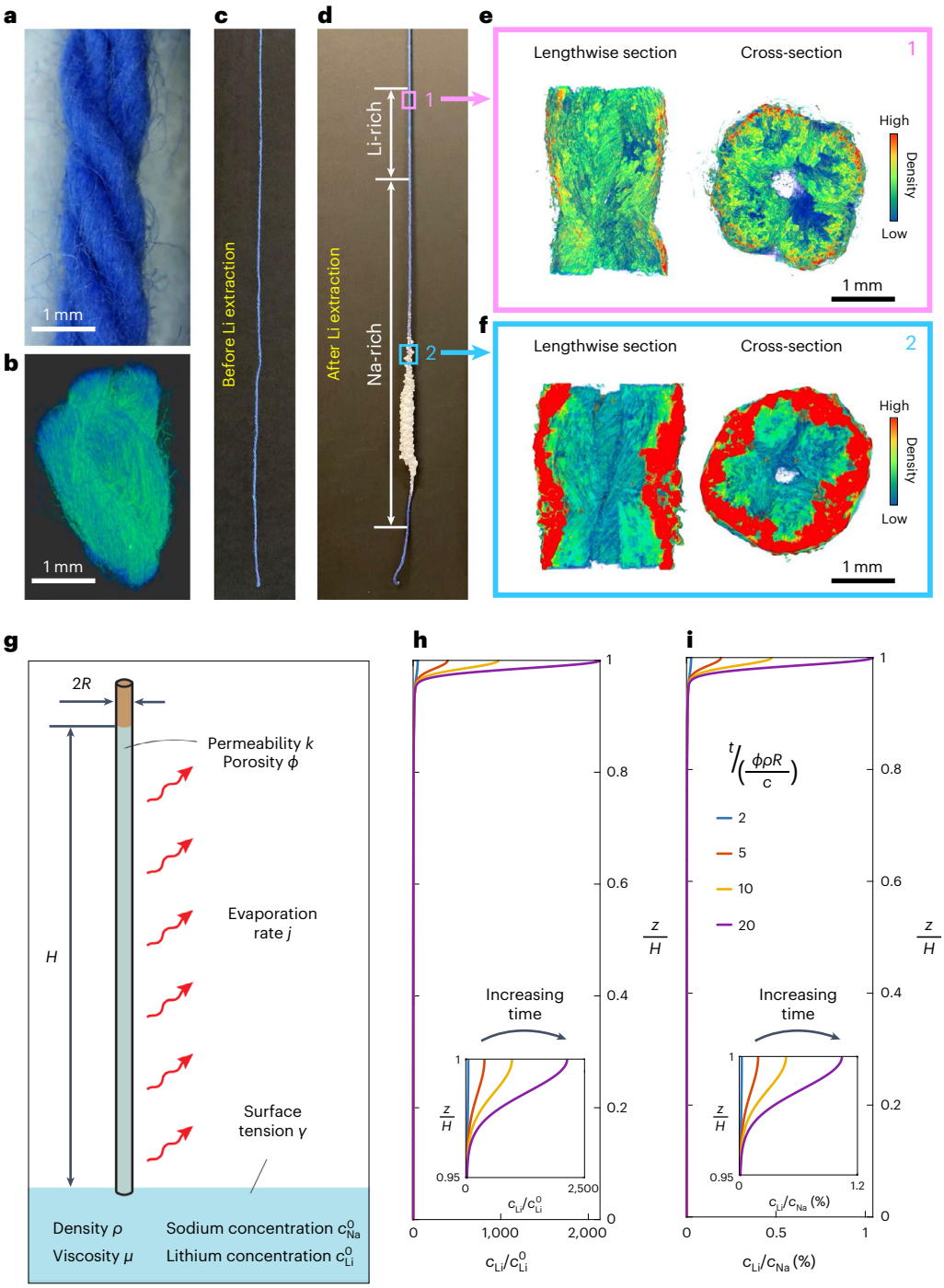


**Fig. 2 | Li is concentrated at the top of the fibre crystallizer. a**,**b**, Zoomed optical image (**a**) and a 3D re-constructed image (**b**) show the twisted structure of the fibre crystallizer. **c**,**d**, The plain fibre crystallizer (**c**) and the salt-covered fibre crystallizer after Li extraction from the continental brine (**d**). Thick salt crystals are observed at the bottom 1/3 of the crystallizer, with a measured high concentration of Na, while thin salt layers distributed above that, with an increasing Li percentage towards the top. **e**,**f**, 3D density distribution at site 1 (**e**; pink-boxed site in **d**) and site 2 (**f**; blue-boxed site in **d**). Salt at site 1 (higher along the fibre) has a lower density, while salt at site 2 (lower along the fibre) has a much higher density, indicating that the lighter element, Li, distributed more at the top position while heavier element, Na, distributed more at the bottom. Note that the salt shell was removed before scan. **g**, Schematic of the geometry and parameters considered in the theoretical model. **h**, Prediction of the Li ion concentration as a function of the position inside the crystallizer. **i**, Model prediction of the Li/Na ratio.

We further characterized the salt crystal morphology to understand the dynamics of ion re-distribution and crystal formation. The SEM–EDX investigations of a submillimeter-scale salt cluster can be found in Supplementary Figs. 11 and 12. Moreover, we employed electron energy loss spectroscopy (EELS) combined with S/TEM to investigate the crystal morphology and elemental distribution at the submicron scale. The S/TEM scanning images depict that square-shaped crystals are surrounded by amorphous precipitations (Fig. 3i). A clear boundary can be observed between the two types of solid in the zoom-in scan (Fig. 3j), indicating the presence of two different salt species. The EELS map confirmed this assumption of Na and Li distribution. On the other hand, Cl was present everywhere as a

https://doi.org/10.1038/s44221-023-00131-3

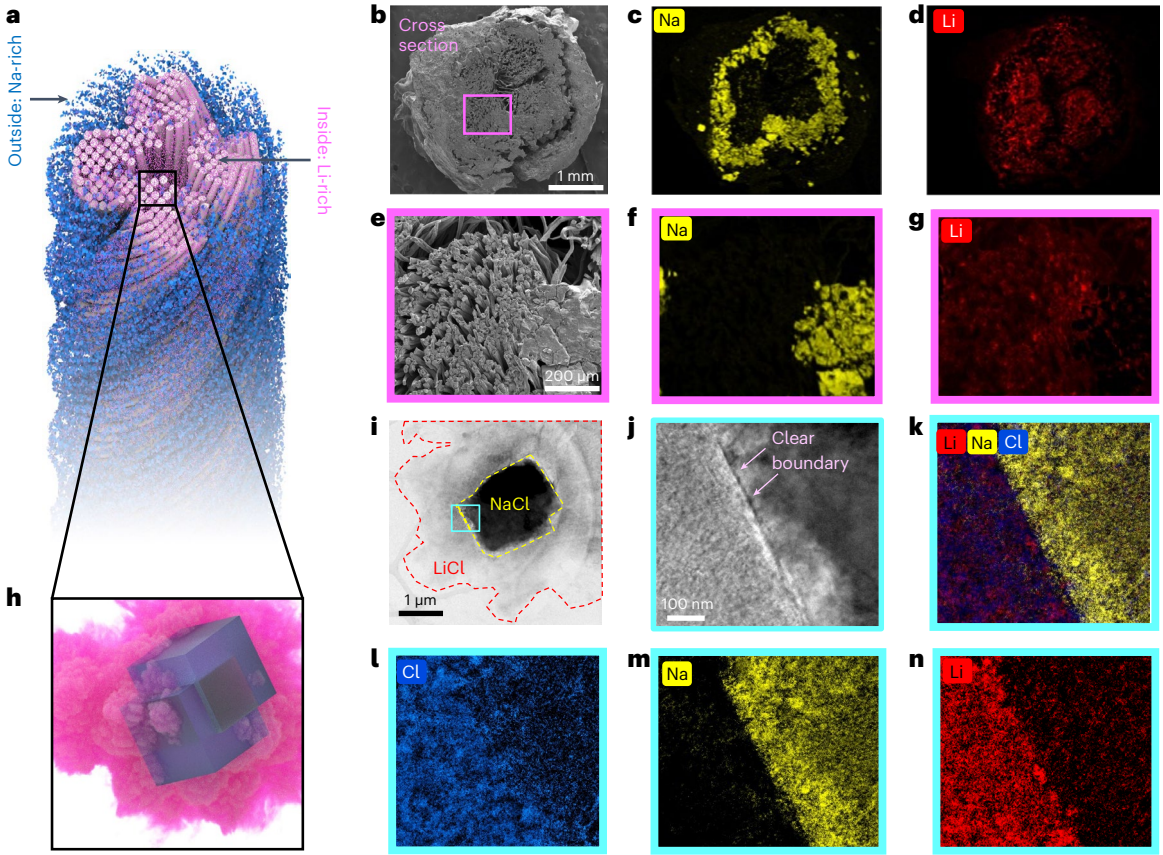


**Fig. 3 | Li is concentrated at the centre of the fibre crystallizer. a**, Schematic showing that Li is concentrated inside the fibre crystallizer, surrounded by the Na-rich salt shell. **b**, SEM image of the cross-section. **c**, Na elemental map from the EDX, showing a circular shape surrounding the crystallizer structure. **d**, Li elemental map from the EDX, showing a dispensed distribution across the crystallizer's cross-section. The Li elementary map was calculated by deducting the Na map from the Cl map (more details in Supplementary Note 2 and Supplementary Figs. 16 and 17)[40,41]. **e**, SEM image of the area between the fibres and salt crystals, pink-boxed in **b**. **f**, Na elemental map from the EDX, showing that only the salt crystals emitted clear Na spectra, while the fibre area showed no Na signal. **g**, Li elemental map from the EDX, showing that Li spectra were widely detected over the fibre areas, with the weakest signal at the bottom-right corner, where the NaCl crystals are located. **h**, Schematic showing that, in the centre Li-rich part, cubic NaCl crystals (blue) act as a core and LiCl form surrounding amorphous salt (pink). **i**, S/TEM image of the salt crystal sampled from the centre. **j**, TEM image of the blue-boxed area in **i**, showing a clear boundary between the two types of salt crystal. **k**, Layered EELS map confirmed two different elemental components aside the boundary. **l**–**n**, Cl (**l**), Na (**m**) and Li (**n**) elemental map from EELS. Cl covered the whole scope, and Na distributed only at the right side of the boundary, while Li distributed mostly at the left side.

counter ion (Fig. 3k–n). More images and discussions can be found in Supplementary Figs. 13–15. These results confirm that central square-shaped crystals are NaCl, while LiCl formed the amorphous precipitations in the peripheral region. The clear boundary between Na and Li suggests a sequential rather than a concurrent crystallization. Because NaCl has a lower solubility and higher concentration, NaCl crystallizes first, while LiCl is prone to precipitate around those NaCl cores gradually when saline water dries out at the location. For the salt particles sampled from the salt shell, we did not observe any EELS spectra of Li. This confirms that most Li are localized inside the mesoporous fibre structure during sequential crystallization.

The 3D twisted fibre crystallizer enables lithium separation by providing a high aspect ratio and a large surface area that allows staged crystallization of different salt species. The twisting structure further enhanced such features, as the spiral structure provides suitable porosities and pathways for saline water to move upwards, drying and crystallizing along the way. We fabricated the structure by firstly spinning the natural cellulose fibres into a tight string, then further twisted four strings together (Fig. 4a,b). For better comparison, cellulose fibres were also aligned to form a linear structure. Compared with the non-twisted control, the single-twisted string lifted water by 102% higher, and the four-string twist crystallizer further increased the lifting by another 57% (Fig. 4c). Such twisting is believed to lead to a larger suction force to lift water higher, and we observed 351% increase in ER by the single twisted string compared with the untwisted string, and 108% increase in ER by the four-string twist (Fig. 4d). Our lab test also showed adding each pair of twisted strands may continue improving water lift by ~10–15% (Supplementary Figs. 18 and 19). Detailed explanation can be found in Supplementary Note 4. Increasing the packing of fibres and strings by twisting would reduce their spacing and thus the effective pore size of the heterogeneous crystallizer. Since the permeability is directly proportional to the characteristic pore size of the medium, twisting could ultimately result in smaller permeabilities and larger values of the lifting height. Except in this section, all experiments were conducted using the four-string twisted structure as a single crystallizer.

We also investigated the scalability of fibre crystallizers by constructing and testing a prototype array consisting of 100 fibre crystallizers (Fig. 5a). Such design can be easily modulated and scaled up for the quick deployment in various lithium production sites, which typically has the most favourable climate conditions for evaporation. Since NaCl would preferentially crystalize at the air–liquid interface, the formed Na-rich salt shells could be harvested by gentle vibration or scraping[34]. In contrast, LiCl stays within the crystallizer[35].

https://doi.org/10.1038/s44221-023-00131-3

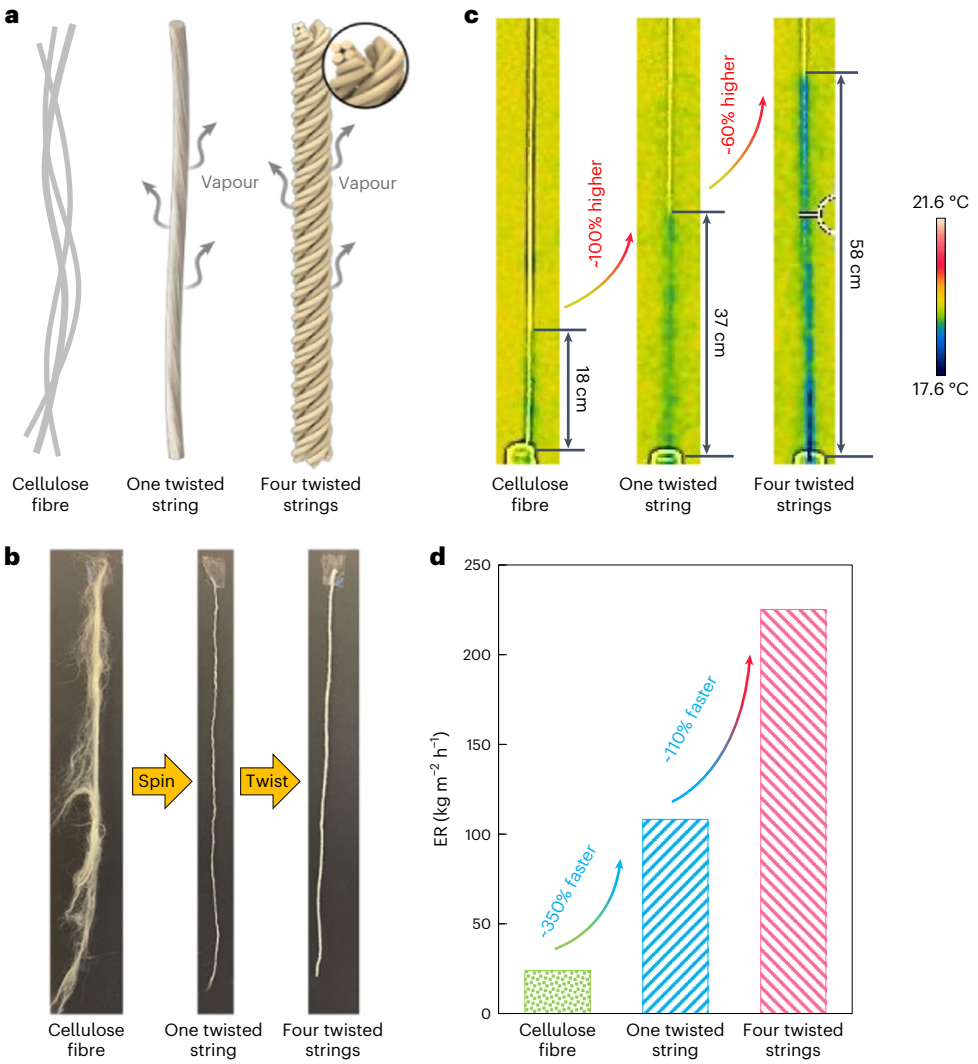


**Fig. 4 | Twist fibre structures achieve high water lifting and faster evaporation from brine water. a**,**b**, Schematic (**a**) and photo (**b**) of the untwisted natural cellulose fibre (diameter 1.2 mm), one twisted string (diameter 1 mm) and four twisted strings (diameter 2 mm). **c**, Forward-looking infrared (FLIR image shows the water lifting heights of the untwisted string (18 ± 1.6 cm), one twisted string (37 ± 1.5 cm) and four twisted strings (58 ± 3.1 cm), indicating that twist structure can increase water lifting height. **d**, ERs of the untwisted string (24 ± 1.2 kg m$^{-2}$ h$^{-1}$), one twisted string (108 ± 15.2 kg m$^{-2}$ h$^{-1}$) and four twisted strings (225 ± 29.7 kg m$^{-2}$ h$^{-1}$), indicating that the twist structure can greatly facilitate water evaporation.

Therefore, a wash–soak method (Fig. 5b) was implemented to further recover the Li-rich salt collected within the crystallizer. In this process, the outer Na-rich salt was washed off by quickly dipping the crystallizer (after outer salt shell was removed) in the water, and the inner Li-rich salt that retained on the crystallizer structure was then collected into a Li-rich concentrate by a thorough soaking. The Li/Na wt. in the recovered concentrate was found to be 55–105% higher than the pre-concentrated Li/Na wt. on the crystallizer structure, indicating an improved overall selectivity of Li over Na (Supplementary Fig. 20). The estimated LiCl production from 100 fibre crystallizers is 2.7 kg per year after crystallization and wash-and-soak harvesting. Such a process may save over 90% of the land use to reach a comparable yearly lithium production capacity of the SQM plant in Chile (~2.4 kt km$^{-2}$ per year)), which has notable advantage for regions with limited space and environmental concerns[33]. A techno-economic analysis is needed to address the trade-off between the enlarged evaporation surfaces by stacking the crystallizers and the extra energy consumption for pumping brine higher, but it is beyond the scope of this study.

## Discussion

The spatially separated crystallization enables effective Li extraction from saline waters without consuming large amounts of energy or chemicals, demonstrating a high efficiency, a low footprint and potential process for scale-up. The process utilizes environmental energy as the driving force and can extract Li faster than the conventional evaporation pond method by an order of magnitude. The natural cellulose fibre-based crystallizer is low-cost and simple to fabricate and dispose, presenting an environmentally friendly method for lithium recovery. Further studies are needed to better understand the crystallization and separation mechanisms, and new materials and devices can be developed to improve separation selectivity and scalability. In this study we focused on the understanding of the ion crystallization process of LiCl via chemical analysis and in situ characterization, as for current evaporation pond operations, other ions such as $Mg^{2+}$ and $Ca^{2+}$ are removed first before the final step of the most difficult monovalent ion separation. Further studies should investigate the potential interferences and removals of other ions present in natural waters to potentially simplify the current long trains of evaporation

https://doi.org/10.1038/s44221-023-00131-3

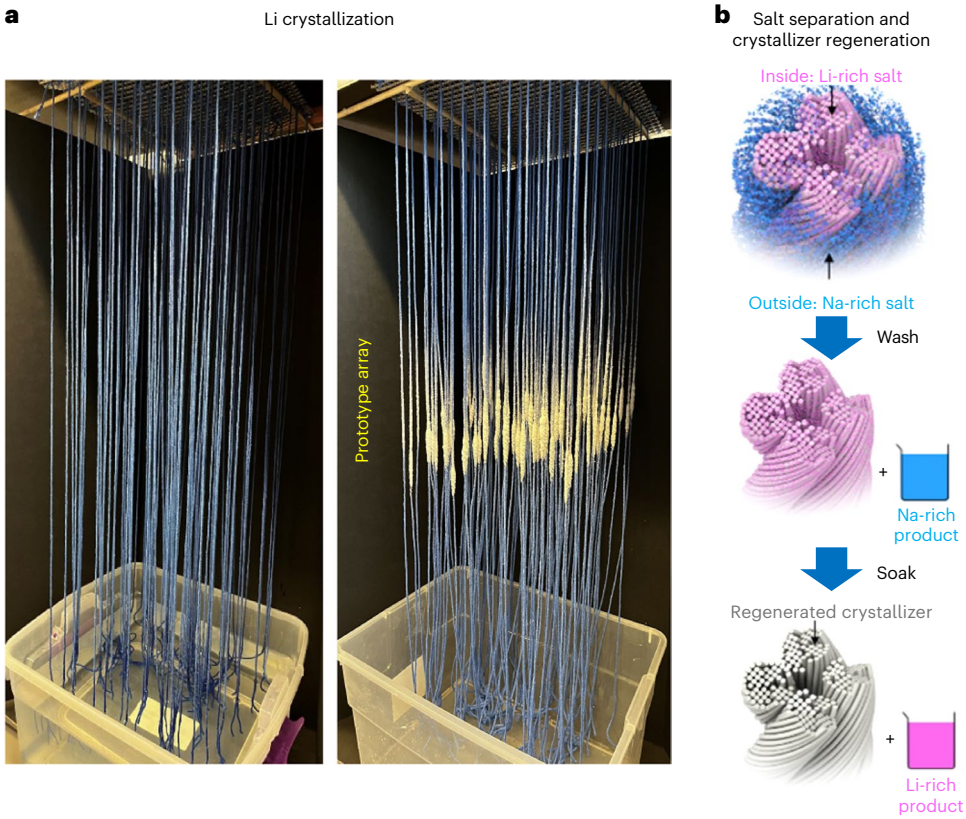


**Fig. 5 | Practical feasibility of the spatial crystallization system using simulated seawater. a**, Photo of a prototype Li extraction array containing 10 × 10 3D spatial crystallizers. Salt crystals are shown on blue cellulose fibre crystallizers. **b**, Li salt recovery by the wash–soak method. After removing the salt shell, the crystallizer was dipped into water to wash off and generate a Na-rich solution. Subsequently, the crystallizer was soaked in clean water bath for Li dissolution and recovery.

process. We also hypothesize this approach could be used to extract other critical minerals such cobalt, nickel or uranium from brines and seawater. Overall, this new approach offers a sustainable pathway for securing the supply of the critical minerals and contributes to a circular low-carbon economy.

## Methods

### Interfacial crystallizer setup and ion analyses

The base material used for fabricating the 3D spatial crystallizer was natural cellulose fibre yarn with a measured diameter of 2 mm. The cellulose fibre yarn was cut into 70 cm pieces and was then soaked in de-ionized (DI) water for 4 h to remove air bubbles in the pores to provide good liquid–solid contact along the whole structure. The fully wetted fibre crystallizer was then arranged vertically with the bottom ~3 cm soaked in the saline water source with continuous replenishment during the experiment. After an extraction cycle, the crystallizer was cut into 2–4 cm pieces along the height and dried in a vacuum oven at 40 °C for over 24 h to fully remove the moisture. The easy-peeling salt shells were removed from the structure and dissolved in DI water for tests. Each individual crystallizer piece was also soaked in DI water separately for over 24 h to guarantee release of all ions into the solution. The water samples were then diluted appropriately, and the ion concentrations were tested by the inductively coupled plasma (ICP) after filtration by polyvinylidene fluoride syringe filters (25 mm, 0.45 µm). Specifically, the $Li^+$ and $Na^+$ concentrations in all samples were measured by the Thermo Scientific iCAP RQ ICP–MS. For system operated with synthetic brine, the samples were operated in the standard (STD) mode with 1,550 W plasma power and a carrier flow of 1.1 l $min^{-1}$ nebulizer gas. Samples with high salinity and low lithium concentration were measure in kinetic energy discrimination (KED) mode which uses a He collision Q-cell to remove interferences and allow low-mass ions such as Li to be detected accurately. To avoid errors caused by dilution, duplicate samples with different dilution ratios were tested for each sample.

### ER measurement

The ER was calculated on the basis of the water loss of the reservoir. The reservoir containing DI water was placed on an electronic scale with real-time weight recording on a computer[36]. The whole system was placed in an environmental chamber (Controlled Environment Room, EGC) with controllable temperature and RH. The mass of the remaining water was recorded every 5 min, and the mass ($y$ axis) was ploted against time ($x$ axis), where the slop of the plot was ER with a unit of g $min^{-1}$. The projected area of evaporators were also recorded. The ER for dark condition was tested under the ambient dark lab condition without sunlight exposure or wind assistance. The ER for 1 sun condition was tested under the synthetic sunlight from a solar simulator with 300 W Xe-arc lamps (Newport), but without any wind assistance[35]. The ER for 1.5 m $s^{-1}$ wind was tested under a measured wind speed of 1.5 m $s^{-1}$ that was generated from a commercial table fan, but without any sunlight exposure[37]. All the tests were conducted with an ambient temperature of ~22 °C and an RH of 22%. For all the test, the blank reference of evaporation from the reservior solely without any evaporator were also measured. The final ER for all the conditions were calculated by subtracting the blank reference.

### Advanced material characterizations

The porosity of the crystallizer was measured by the water volume. The crystallizer was cut into sections with different lengths, where the weight was measured as $m_0$. Then each section was immersed into DI water to fill all the pores. After removing the crystallizer from water,

the weight was measured as $m_{wet}$. The absorbed water volume can be calculated by:

$$V_{H2O} = \frac{m_{wet} - m_0}{\rho}$$

where $\rho$ represents the density of $H_2O$, which is 0.998 g cm$^{-3}$ (20 °C). The volume of the crystallizer ($V_{crystallizer}$) was calculated by assuming the crystallizer as a cylinder. Then for different crystallizers with varying lengths, we plotted $V_{crystallizer}$ versus $V_{H2O}$. The porosity is considered as the slope, which is 83.71%.

In the micro- to millimetre scale, the morphology of the crystallizer before and after the Li extraction cycle was characterized by an environmental scanning electron microscope (SEM). Elementary maps for Na and Cl were acquired using the energy-dispersive X-ray spectroscopy (EDS) equipped in the same instrument[38]. However, the characteristic X-rays of Li are of too low energy (~55 eV) to be detected by EDS, so conventional elemental analysis/imaging methods can hardly detect Li salts. Therefore, the elemental map of Li was adjusted by deducting the Na map from the Cl map, assuming that, if Na is absent, Li should be the counter ion pairing with Cl and balance the electric charge in salt crystals. To obtain accurate mineral separation results, we did not introduce other ions in these experiments (details in the next section).

In the submicrometre scale, the characterization of the salt crystals was conducted by the EELS combining with the scanning/transmission electron microscopy (S/TEM). The sensitivity of EELS for Li is sufficiently high (0.2 wt.%) with the excitation of low energy loss appearing at 55 eV (Li K-edge). So the elementary map for Li, Na and Cl in nanometres was directly acquired from the EELS, which revealed the clear distribution of Li and Na salts and supported the analysis of crystal formation.

### Salt species composition analysis

Two synthetic saline water conditions were used for testing the Li extraction. Seawater condition was based on the typical ocean composition: $c(Li^+)$ = 0.18 ppm and $c(Na^+)$ = 10,800 ppm. Brine condition was based on the typical geothermal brine composition at Salar de Atacama, Chile: $c(Li^+)$ = 1,500 ppm and $c(Na^+)$ = 76,000 ppm.

After a Li extraction process from the brine condition, the salt density along the 3D spatial crystallizer was characterized by 3D X-ray images generated by Zeiss Xradia 520 Versa High-resolution 3D X-ray tomography Microscope. Two 2 cm sections were taken from both Li-rich and Na-rich region from the 3D spatial crystallizers for analysis, as boxed in Fig. 2d. Avizo software was used to reconstruct 3D volumes automatically or manually from 2D scan data, and used for data integration, visualization and animation of the scan data.

### Lithium recovery and selectivity

Lithium recovery was tested on the basis of a 10 × 10 crystallizer array, which had a projected area of 225 cm$^2$. The gap between two crystallizer fibres was 1.5 cm. The test was conducted under the ambient temperature of 22 °C, RH of 22% and wind speed of 1.5 m s$^{-1}$, and the solution employed was the typical brine composition at Salar de Atacama, Chile.

During the test, the 10 × 10 array was placed in a container containing 2,000 ml brine, where the initial and end mass and duration time were recorded. After the operation, three parallel crystallizers were collected from different array positions. Each collected crystallizer was immediately divided into four segments, from top to bottom, each with a length of 12 cm. Then the topmost segment was further divided into three subsegments, with a length of 3, 3 and 6 cm. The salt shell was peeled off for each subsegment, and then the crystallizer and salt shell were fully dissolved in 25 ml DI $H_2O$. The Li and Na concentrations were analysed for all the samples. The total Li mass was calculated over the whole crystallizer (with the salt shell). The Li recovery for each sector was calculated by dividing the Li mass in the crystallizer by the total Li mass (equation (1)). The Li/Na percentage was calculated for each crystallizer segment. At the same time, the selectivity was calculated by dividing the Li/Na percentage in the crystallizer by the Li/Na percentage in the initial brine solution (equation (2)).

$$\text{Li recovery} = \frac{\text{Li in crystallizer}}{\text{Total Li}} \times 100\% \quad (1)$$

$$\text{Selectivity} = \frac{\frac{\text{Li}}{\text{Na}}\% \text{ in crystallizer}}{\frac{\text{Li}}{\text{Na}}\% \text{ in initial brine}} \quad (2)$$

For different recovery lengths, the Li recovery was obtained by integrating the Li recovery over different segments of the whole crystallizer. While the Li/Na wt. for a certain length was calculated with the average Li/Na wt. among different sections. The mean and standard deviation for Li recovery and selectivity were calculated on the basis of the three parallel samples.

### Mechanistic model development

A comprehensive model was developed for the transport of ions inside a slender, porous cylinder continuously drawing a liquid solution from a reservoir and evaporating along its length (Fig. 2g). Continuous evaporation along the length of a high aspect ratio structure provides high surface area for increased concentration enhancement from water loss. Within the slender crystallizer, the fluid flow is perpendicular to the evaporative flux, and the porous medium does not partially fill with air pockets due to the continuous liquid flux from the reservoir. As elaborated earlier, the theory accounts for the transport of ions through advection (which is induced by ambient evaporation) and diffusion, predicting the concentration of Na or Li ions as a function of time t and the position z along the water lifting height, $H$. The one-dimensional model considers the transport equation for a species of concentration $c$:

$$\frac{\partial c}{\partial t} + \frac{\partial}{\partial z}(vc) = D\frac{\partial^2 c}{\partial z^2} \quad (4)$$

where $D$ is the diffusivity of the species through the porous cylinder and $v$ is the vertical velocity induced by evaporation. An expression for $v$ can be obtained from the Darcy equation for fluid flow in porous media, yielding

$$v(z) = v_0\left(1 - \frac{z}{H}\right) \quad (5)$$

The characteristic fluid velocity is $v_0 = 2jH/(\rho R)$, in which $j$ is the ER, $\rho$ is the solution density, and $R$ is the radius of the crystallizer. Furthermore, the height $H$ of the water column (Fig. 2g) is set by the competition between capillary forces, which promote the liquid rise, which is defined as $H = \gamma\sqrt{\phi}/\left(\rho g\sqrt{k}\right)$. The permeability $k$ and porosity $\phi$ are intrinsic properties of the material of the crystallizer, while $g$ and $\gamma$ are the gravitational acceleration and the surface tension between air and water, respectively. The 1D model assumes $R/H \ll 1$ as in the experiments.

The model equations are governed by a single dimensionless parameter, the Péclet number $\mathrm{Pe} = jH^2/(\rho RD)$, which measures the relative predominance of advective and diffusive transport effects and has already been identified in other salt precipitation problems[39]. Additionally, the ratio of ion concentrations also depends on the saturation parameter $c^0_{Na}/c^{sat}_{Na}$ of sodium. The governing equations are solved numerically using an in-house finite-volume method with a two-stage implicit–explicit Runge–Kutta time integrator. Additionally, asymptotic analysis shows that, at high Péclet numbers $\mathrm{Pe} \gg 1$, the leading order solution for the concentration of any ion is $c(z,t)/c^0 = H/(H-z)$ for $0 \le z/H \le 1 - e^{-2t/(\phi\rho R/j)}$ and $c(z,t)/c^0 = e^{2t/(\phi\rho R/j)}$ for $1 - e^{-2t/(\phi\rho R/j)} \le z/H \le 1$.

## Data availability

All data are presented in the article and its Supplementary Information. Source data are provided with this paper.

## References


1. Goldthau, A. & Hughes, L. Protect global supply chains for low-carbon technologies. *Nature* **585**, 28–30 (2020).
2. Greim, P., Solomon, A. A. & Breyer, C. Assessment of lithium criticality in the global energy transition and addressing policy gaps in transportation. *Nat. Commun.* **11**, 1–11 (2020).
3. Sun, X., Liu, Z., Zhao, F. & Hao, H. Global competition in the lithium-ion battery supply chain: a novel perspective for criticality analysis. *Environ. Sci. Technol.* **55**, 12180–12190 (2021).
4. Raw materials for a truly green future. *Nat. Rev. Mater.* **6**, 455 (2021).
5. Miatto, A., Wolfram, P., Reck, B. K. & Graedel, T. E. Uncertain future of American lithium: a perspective until 2050. *Environ. Sci. Technol.* **55**, 16184–16194 (2021).
6. Lithium. *TRADING ECONOMICS* https://tradingeconomics.com/commodity/lithium (2023).
7. Azevedo, M., Baczynska, M., Hoffman, K. & Krauze, A. Lithium mining: how new production technologies could fuel the global EV revolution. *McKinsey & Company* https://www.mckinsey.com/industries/metals-and-mining/our-insights/lithium-mining-how-new-production-technologies-could-fuel-the-global-ev-revolution (2022).
8. Jaskula, B.W. USGS: 2015 Minerals Yearbook: lithium [advanced released]. https://minerals.usgs.gov/minerals/pubs/commodity/lithium/myb1-2015-lithi.pdf (2017).
9. Yao, S. Lithium costs up in 2021, continuing to surge in 2022. *S&P Global Market Intelligence*. https://www.spglobal.com/marketintelligence/en/news-insights/research/lithium-costs-up-in-2021-continuing-to-surge-in-2022 (2022).
10. Murodjon, S., Yu, X., Li, M., Duo, J. & Deng, T. Lithium recovery from brines including seawater, salt lake brine, underground water and geothermal water. *Thermodyn. Energy Eng.* https://doi.org/10.5772/intechopen.90371 (2020).
11. He, X., Kaur, S. & Kostecki, R. Mining lithium from seawater. *Joule* **4**, 1357–1358 (2020).
12. Grosjean, C., Herrera Miranda, P., Perrin, M. & Poggi, P. Assessment of world lithium resources and consequences of their geographic distribution on the expected development of the electric vehicle industry. *Renew. Sustain. Energy Rev.* **16**, 1735–1744 (2012).
13. Yang, S., Zhang, F., Ding, H., He, P. & Zhou, H. Lithium metal extraction from seawater. *Joule* **2**, 1648–1651 (2018).
14. Xu, J. et al. A green and sustainable strategy toward lithium resources recycling from spent batteries. *Sci. Adv.* **8**, eabq7948 (2022).
15. *Lithium Market—Industry Analysis and Forecast (2022–2029)* (Maximize Market Research Pvt, 2019).
16. Sociedad Química y Minera de Chile S.A. (*SQM 2021): Annual Reports* https://ir.sqm.com/English/financials/annual-reports/default.aspx (2021).
17. Gutiérrez, J. S., Navedo, J. G. & Soriano-Redondo, A. Atacama imperilled by lithium mining. *Nature* https://doi.org/10.1038/d41586-018-05233-7 (2018).
18. Lèbre, É. et al. The social and environmental complexities of extracting energy transition metals. *Nat. Commun.* https://doi.org/10.1038/s41467-020-18661-9 (2020).
19. Amoatey, P. et al. A critical review of environmental and public health impacts from the activities of evaporation ponds. *Sci. Total Environ.* **796**, 149065 (2021).
20. Safari, S., Lottermoser, B. G. & Alessi, D. S. Metal oxide sorbents for the sustainable recovery of lithium from unconventional resources. *Appl. Mater. Today* **19**, 100638 (2020).
21. Stringfellow, W. T. & Dobson, P. F. Technology for lithium extraction in the context of hybrid geothermal power. *Proc. 46th Work. Geotherm. Reserv. Eng.* **46**, 1–20 (2021).
22. Li, X. et al. Membrane-based technologies for lithium recovery from water lithium resources: a review. *J. Memb. Sci.* **591**, 117317 (2019).
23. Liu, G., Zhao, Z. & Ghahreman, A. Novel approaches for lithium extraction from salt-lake brines: a review. *Hydrometallurgy* **187**, 81–100 (2019).
24. Sun, Y., Wang, Q., Wang, Y., Yun, R. & Xiang, X. Recent advances in magnesium/lithium separation and lithium extraction technologies from salt lake brine. *Sep. Purif. Technol.* **256**, 117807 (2021).
25. Zhao, X., Yang, H., Wang, Y. & Sha, Z. Review on the electrochemical extraction of lithium from seawater/brine. *J. Electroanal. Chem.* **850**, 113389 (2019).
26. Parsa, N., Moheb, A., Mehrabani-Zeinabad, A. & Masigol, M. A. *Recovery of Lithium Ions from Sodium-Contaminated Lithium Bromide Solution by Using Electrodialysis Process. Chemical Engineering Research and Design* vol. 98 (Institution of Chemical Engineers, 2015).
27. Hoshino, T. Preliminary studies of lithium recovery technology from seawater by electrodialysis using ionic liquid membrane. *Desalination* **317**, 11–16 (2013).
28. Warnock, S. J. et al. Engineering Li/Na selectivity in 12-Crown-4-functionalized polymer membranes. *Proc. Natl Acad. Sci. USA* **118**, 1–8 (2021).
29. Habata, Y., Ikeda, M. & Akabori, S. Lithium ion selective dibenzo-14-crown-4 possessing a phosphoric acid functional group as a pendant. *Tetrahedron Lett.* **33**, 3157–3160 (1992).
30. Hano, T., Matsumoto, M., Ohtake, T., Egashira, N. & Hori, F. Recovery of lithium from geothermal water by solvent extraction technique. *Solvent Extr. Ion Exch.* **10**, 195–206 (1992).
31. Swain, B. Separation and purification of lithium by solvent extraction and supported liquid membrane, analysis of their mechanism: a review. *J. Chem. Technol. Biotechnol.* **91**, 2549–2562 (2016).
32. Yim, C.-H. & Abu-Lebdeh, Y. A. Connection between phase diagram, structure and ion transport in liquid, aqueous electrolyte solutions of lithium chloride. *J. Electrochem. Soc.* **165**, A547–A556 (2018).
33. Report, O. & Atacama, S. D. E. Technical Report Summary Operation Report Salar de Atacama (2022).
34. Kuznetsov, G. V. et al. Evaporation modes of LiBr, $CaCl_2$, LiCl, NaCl aqueous salt solution droplets on aluminum surface. *Int. J. Heat Mass Transf.* **126**, 161–168 (2018).
35. Lu, L. et al. Unbiased solar $H_2$ production with current density up to 23 mA $cm^{-2}$ by Swiss-cheese black Si coupled with wastewater bioanode. *Energy Environ. Sci.* **12**, 1088–1099 (2019).
36. Chen, X. et al. Sustainable off-grid desalination of hypersaline waters using Janus wood evaporators. *Energy Environ. Sci.* **14**, 5347–5357 (2021).
37. Zheng, S. et al. Upscaling 3D engineered trees for off-grid desalination. *Environ. Sci. Technol.* **56**, 1289–1299 (2022).
38. Jiang, J., Chen, X., Chen, X. & Ren, Z. J. Energy-efficient microbial electrochemical lignin and alkaline hydroxide recovery from DMR black liquor. *Resour. Conserv. Recycl.* **186**, 106529 (2022).
39. Guglielmini, L., Gontcharov, A., Aldykiewicz, A. J. & Stone, H. A. Drying of salt solutions in porous materials: intermediate-time dynamics and efflorescence. *Phys. Fluids* **20**, 077101 (2008).
40. Li, C. et al. Mapping techniques for the design of lithium-sulfur batteries. *Small* **18**, 1–14 (2022).
41. Adhitama, E. et al. Pre-lithiation of silicon anodes by thermal evaporation of lithium for boosting the energy density of lithium ion cells. *Adv. Funct. Mater.* **32**, 2201455 (2022).


## Acknowledgements

The authors appreciate the support from Princeton Catalysis Initiative (PCI), and we acknowledge the use of Princeton's Imaging and Analysis Center, which is partially supported through the Princeton

Center for Complex Materials (PCCM), a National Science Foundation (NSF)-MRSEC programme (DMR-2011750). F.T.-C. and S.Z. gratefully acknowledge the Distinguished Postdoctoral Fellowships from the Andlinger Center for Energy and the Environment.

## Author contributions

X.C. conceived the initial idea with the input from group members. X.C., M.Y., S.Z., Z.J.R. and L.H. contributed to the experimental design. Z.J.R. supervised the study. X.C., M.Y. and S.Z. conducted materials preparation and system operation. F.T.-C. and H.A.S. carried out model development. X.C., G.C. and N.Y. conducted material characterization. X.C., M.Y. and S.Z. contributed to experimental analysis. X.C. and Q.D. contributed to schematics design. X.C., M.Y., F.T.-C. and Z.J.R. wrote the paper, and all authors commented on the final manuscript.

## Competing interests

X.C., S.Z. and Z.R. are authors on a patent application (PCT/US22/50915) for fibre evaporators. The other authors declare no competing interests.

## Additional information

**Supplementary information** The online version contains supplementary material available at https://doi.org/10.1038/s44221-023-00131-3.

**Correspondence and requests for materials** should be addressed to Zhiyong Jason Ren.

**Peer review information** *Nature Water* thanks Ping He and the other, anonymous, reviewer(s) for their contribution to the peer review of this work.